Atmospheric Environment 252 (2021) 118340

Contents lists available at ScienceDirect

Atmospheric Environment

journal homepage: http://www.elsevier.com/locate/atmosenv

Characteristics of atmospheric CO_2 fluxes and the estimation of their potential sources around Boseong Standard Weather Observatory (BSWO)

Changhyoun Park [a], Young-Tae Lee [b], Soon-Hwan Lee [c,*]

[a] Institute of Environmental Studies, Pusan National University, Busan, 46241, South Korea
[b] Operational Systems Development Department, National Institute of Meteorological Sciences, Seogwipo-si, Jeju-do, 63568, South Korea
[c] Department of Earth Science Education, Pusan National University, Busan, 46241, South Korea

HIGHLIGHTS

- The CO_2 concentration and flux measurements at multiple levels on avery tall tower.
- Biogenic features of fluxes on each measurement level.
- Flux directionality analysis with GIS technique finds potential sources within footprints.
- Comparison between the top-down (flux measurements) and bottom-up (emission dataset) approaches.

ABSTRACT

We report the characteristics of the mixing ratios and fluxes of atmospheric carbon dioxide, observed in the period from July 2015 to December 2019. Measurements were noted for three different levels (60 m, 140 m, and 300 m above ground level (a.g.l.)) on a very tall (~300 m) tower in the Boseong Standard Weather Observatory (BSWO), located at the center of barley–rice double-crop fields in Boseong-gun, Jeolla-do, South Korea. The averaged CO_2 mixing ratios show 420.7 ± 18.8 (60 m), 410.9 ± 16.7 (140 m) and 403.4 ± 16.7 ppm (300 m). The mixing ratios measured at the 140-m and 300-m heights display a typical seasonal pattern that is lower in the summer due to vegetation uptake and higher in the winter due to plant decaying combined with fossil-fuel emissions, but those at 60 m presented higher values in the spring and autumn, mainly owing to agricultural activities. During the study period, the averaged CO_2 fluxes are −0.28 ± 8.81 (60 m), 0.34 ± 8.08 (140 m), and 0.79 ± 9.08 µmol m^{-2} s^{-1} (300 m). The monthly averaged fluxes show two dominant negative peaks, one in April and another in August, mainly caused by CO_2 uptake during the barley and rice growing periods, respectively. The fluxes represent a strong correlation between daytime solar radiation and photosynthesis and between nighttime air temperatures and respiration. Directional analysis of the fluxes revealed dominant anthropogenic CO_2 sources from not only the main industrial areas in the NE directions using geographic information system (GIS), but also from the aquaculture industry in the SE. We compare our measured CO_2 fluxes (top-down) with a few bottom-up emissions datasets, which reveal an underestimation of the range from 31% to 69% within the footprint areas. The application of direct measurements of CO_2 fluxes, combined with estimation of potential vicinity sources, can be a useful tool to detect local unknown or missing sources and supplement the gap between top-down and bottom-up approaches.

1. Introduction

Interactions of mass, energy, and momentum between the Earth's surface and atmosphere occur continuously and adversely affect life on Earth. The increase in human activities, such as fossil fuel combustion and changes in the land-use and land-cover (LULC), has resulted in an increase in mixing ratios of carbon dioxide (CO_2) and other greenhouse gases (GHGs) in the atmosphere, which significantly contribute to climate change and worsen global warming (IPCC, 2013). Therefore, anthropogenic emissions are an essential concern for Earth's sustainability.

Various studies have been conducted to better understand the carbon interactions between the surface and atmosphere. To estimate the carbon budget between the terrestrial ecosystem and the atmosphere, researchers generally use two approaches: bottom-up and top-down approaches. In the bottom-up approach, statistical information from individual anthropogenic inventories, including industrial, residential, commercial, and transport sectors, is collected by administrative units, combined with the carbon content of fuel types, and integrated to produce a large bulk inventory scale (e.g., Gurney et al., 2009; Le Quere et al., 2014; Asefi-Najafabady et al., 2014). In contrast, the top-down approach uses measurement data, including inverse modeling and flux

* Corresponding author.
E-mail address: withshlee@pusan.ac.kr (S.-H. Lee).

https://doi.org/10.1016/j.atmosenv.2021.118340
Received 15 December 2020; Received in revised form 4 March 2021; Accepted 8 March 2021
Available online 13 March 2021

measurements. The former is a large-scale predictive atmospheric transport modeling technique that estimates a priori initial mixing ratios and fluxes while preserving the consistency between the observations and simulated results (e.g., Tans et al., 1990; Turnbull et al., 2011; Peylin et al., 2005). The latter is mostly carried out to quantify the local- or neighborhood-scale (102–104 m) interactions between the surface and the atmosphere. Over the last few decades, various flux measurement networks (e.g., FLUXNET-ORNL, AmeriFlux, AsiaFlux, OzFlux, and ChinaFlux (Baldocchi et al., 2001; Falge et al., 2002) have established a combination system of eddy covariance (EC) with infrared gas analyzers (IRGAs) for CO_2 and H_2O. This system is used to observe CO_2 fluxes and quantify the terrestrial biospheric carbon cycle based on the calculated net ecosystem exchange (NEE) in vegetation-dominated areas.

The spatial coverage or scale of flux measurements can be determined by the footprint probability (FP) function, which is a combination of the source area of the measured flux in relation to its spatial extent and the intensity distribution (Horst and Weil, 1992). The higher the measurement level, the larger the spatial coverage. To extend the spatial scale, a higher measurement point should be attained. This condition is highly demanded particularly in heterogeneous areas, where the constant flux layer, i.e., the layer on which the EC measurement point should be placed, is generally located at higher levels. The measurement of the CO_2 flux (hereafter, FCO_2) is difficult because of the heterogeneity of Earth's surface, complexity of source and sink mechanisms, variability in atmospheric turbulence, and limitations of the measurement technique. Flux measurements at a very tall tower are rare mainly owing to the high cost of equipment installation and management. The first tall (610-m) tower site for long-term CO_2 exchange monitoring was established in Wisconsin, USA in 1994 (Bakwin et al., 1995, 1998; Davis et al., 2003; Yi et al., 2000). Recently, tall tower systems have also been constructed in urban areas to monitor anthropogenic sources, as well as to evaluate and certify anthropogenic CO_2 emissions (e.g., Grimmond et al., 2004; Nemitz et al., 2002; Park and Schade., 2016; Velasco et al., 2005; 2013; Liu et al., 2012).

South Korea also has several flux measurement sites as a part of the AsiaFlux network, including Seto mixed forest (FLUXNET site code: SMF), Gwangreung deciduous forest (GDK), Taehwa broadleaf forest (TBK), Haenam paddy field (HPK), Haenam farmland (HFK), and Gimje rice paddy (GRK). The National Institute of Meteorological Sciences (NIMS) of the Korea Meteorological Administration (KMA) established a 300-m-tall tower observation system at Boseong-gun, Jeollanam-do, at the edge of the southern coastal area of the Korean Peninsula in December 2013. The Boseong Standard Weather Observatory (34°45′48″ N, 127°12′53″ E; hereafter, BSWO) is a state-of-the-art 3D weather observatory, designated as a WMO-CIMO Testbed for the integration of the 3D weather observation system. The advantages of the installation of the tower for climate and environmental monitoring include (1) a carbon tracking system to verify the GHG inventory, (2) a national standard agricultural weather observation site, and (3) a tall tower for the monitoring of the micrometeorology, air pollution, and radiative flux at different levels.

Several studies have used measurement data from BSWO. NIMS/KMA reported a few applications of tower measurements from a micrometeorological perspective. They investigated the planetary boundary layer and validated remote-sensing data and a numerical weather forecasting system using tower data by NIMS. Lim and Lee (2019) investigated the vertical structure of sea breeze and found that the intensity of the inversion layer above 40 m was the strongest in westerly winds. The measured tower data have also been used to improve numerical simulations, such as KMA's currently operational WRF-PAFOG model (Kim et al., 2020) and Joint UK Land Environment Simulator (JULES; Kim et al., 2019); the data have also been used to verify the corrections of remote sensing data, such as unmanned aerial vehicles (Kim and Kwon, 2019).

However, these previous studies mainly focused on meteorological analyses and short-term preliminary tests. Focusing on CO_2, in this study, we determine the characteristics of the CO_2 mixing ratios and fluxes based on long-term (~5-yr) measurements acquired from multiple levels. We present (1) the temporal and vertical characteristics of the mixing ratios and fluxes of CO_2, (2) their relationships with solar radiation and air temperature, associated with photosynthesis and respiration, (3) the wind direction dependency of the fluxes, and (4) a comparison of the anthropogenic emissions between top-down and bottom-up approaches.

2. Method

2.1. Site description and tower setup

Fig. 1 shows the distribution of LULC around the tower site, with potential buildings for anthropogenic sources, retrieved by geographic information system (GIS) (QGIS, version 3.10). The measurement tower is installed in an observation field (area of ~154,500 m^2; sea surface level of ~3 m; Fig. 1) in the middle of flat homogeneous barley–rice double-crop paddy fields. Around the site, the Namhae coast is located at ~1.5 km in the SE direction, mountains (576 m) are located to the north, stretching to the NE, and narrow valleys are located to the E and W. Residential houses and agricultural warehouses are mainly located at the mountain foot from the W to NE directions. Two single-lane roads cross the area from the northeast–southwest directions at ~1.5 km to the north. Tens of small agricultural and industrial factories are distributed throughout this area (Fig. 1). The study domain spans two administrative units (called gun), including Boseong-gun and Goheung-gun, in which GIS retrieved 18,324 and 4,970 total building polygons, respectively, specifically within the footprint area of 300 m. Table S1 lists the usability and number of buildings retrieved.

The height of the tower is 307 m a.g.l. Various meteorological equipment is deployed at 11 levels at 10, 20, 40, 50, 80, 100, 140, 180, 220, 260, and 300 m. At each level, booms are installed in three different directions, i.e., south, northwest, and northeast, at 120° intervals; these booms are equipped with temperature (model 5628, Fluke) and humidity sensors (model HMP155A, Vaisala), encapsulated by a radiation shield and a 2D sonic anemometer (model UA-2d, Thies Clima). A net radiation sensor (model CNR4, Kipp&Zonen) is installed at 60 m, 140 m, and 300 m, where a 3D sonic anemometer (model CSAT3A, Campbell Sci.) is installed, combined with an IRGA for CO_2/H_2O measurements. An enclosed system (model Li-7200RS, Licor) is installed at the 60-m level, and two closed-systems (model EC-155, Campbell Sci.) are set up at 140 m and 300 m.

2.2. Data processing

In this study, we used data measured during the study period from July 2015 to December 2019. The data acquired from the sonic anemometers and CO_2/H_2O analyzers were recorded at 20 Hz on dataloggers (model CR3000, Campbell Sci) and then saved to a data server via wireless transfer. We used the EddyPro (Licor; version 7.0.4) software to conduct quality control for processing the raw data of turbulence and conducting quality checks based on WMO guidelines. The R-language software (R Core Team, 2014) was used for analyzing the 30-min averaged data. During the study period, several long-term (>10 days) measurement breaks occurred due mainly to systematic failures. The break periods at each measurement level are reported in Table S2.

The double rotation method was used to correct the anemometer axis tilt to mean streamlines, nullifying the averaged cross-stream and vertical components during a half-hour period based on the findings of Wilczak et al. (2001). The block-averaging or Reynolds averaging method calculated the turbulent fluctuations as individual departures from the mean value of the variable, as suggested by Gash and Culf (1996). In the closed-path system, the gas mixing ratios are always measured with a certain delay to the moment air is sampled at the intake tube. We compensated for the time lag between the IRGA and inlet

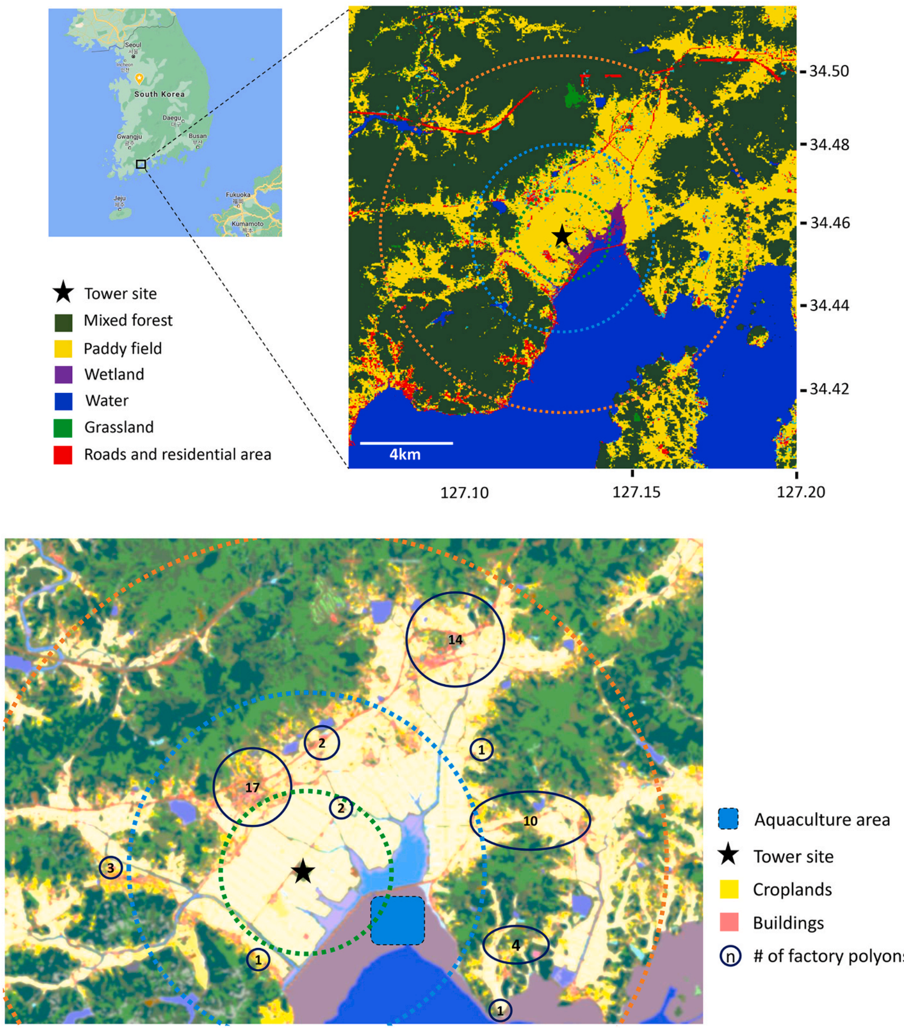

Fig. 1. Distribution of the land cover in the study area (18 km × 18 km; upper panel) and potential anthropogenic sources. The numbers in black circles indicate the number of factory polygons retrieved by GIS. Green-, blue-, and orange-dotted circles indicate the 2-km, 4-km, and 8-km radii from the tower, respectively. (For interpretation of the references to colour in this figure legend, the reader is referred to the Web version of this article.)

installed adjacent to the anemometer (the length of the PFA tube was 81 cm at 140 m and 86 cm at 300 m). The time lag was determined as the time that maximizes the covariance of two within a window of plausible time lags (Fan et al., 1990). To convert the gas mixing ratios to mixing ratios in the closed-path system, we applied the WPL correction (Webb et al., 1980), which is an alternative method to account for the air density fluctuation due to water vapor (Ibrom et al., 2007).

For the statistical tests for raw data screening, we performed despiking, drop-outs, and skewness and kurtosis tests, with the configurable parameters used by Vickers and Mahrt (1997). Non-stationarity can be introduced depending on the meteorological conditions; thus, we performed the steady-state test and the well-developed turbulence test using a quality flagging system based on the method of Mauder and Foken (2006). In the frequency range of the raw data, we applied the low-frequency spectral correction (Moncrieff et al., 2004) to the high-frequency dissipation range and the high spectral correction (Moncrieff et al., 1997) to the low-frequency turbulence production range. Table 1 reports the collection ratio of 30-min data.

After completing quality assurance and quality control (QA/QC), the 30-min CO_2 fluxes were calculated by the equation:

$$F_{CO_2} = \overline{\rho_d} \times \overline{w' \chi'_{CO_2}} \qquad (\text{unit}: \ \mu mol\ m^{-2} s^{-1}) \tag{1}$$

where $\overline{\rho_d}$ is the average of air density, and $\overline{w'\chi'_{CO_2}}$ is the averaged covariance of the fluctuation of vertical wind speed (w') and the mole fraction of CO_2 (χ'_{CO_2}).To account for low turbulence conditions, we applied a friction velocity threshold of u* < 0.2 m s^{-1}. We also removed the 30-min flux data for the periods of rain and 24 h after rain. To fill the

Table 1
Collection ratio of the 30-min CO_2 flux data for each crop cultivation stage at all three measurement points.

Crop type	Cultivation stage	Symbol	Collection ratio (%)		
			60-m	140-m	300-m
Barley	Germination (Oct. 30 – Nov. 5)	B1	89.5	36.1	75.9
	Seedling and winter-rest (Nov. 6 – Feb. 27)	B2	79.9	49.2	79.4
	Tillering (Feb. 28 – May 11)	B3	55.4	45.6	75.8
	Ripening (May 12 – May 24)	B4	40.0	20.0	79.2
	Harvesting (May 25 – Jun. 5)	Bh	79.9	44.0	90.5
Rice	Rooting (Jun. 5 – Jun. 10)	R1	39.8	30.3	73.8
	Tillering (Jun. 11 – July 9)	R2	74.9	48.9	84.9
	Elongation (July 10 – Aug. 11)	R3	84.1	55.7	97.4
	Ripening (Aug. 12 – Oct. 19)	R4	97.4	57.1	97.5
	Harvesting (Oct. 20 – Oct. 30)	Rh	97.0	55.3	94.2
Total			74.9	48.9	84.9

gap of fluxes, we adopted the R package of 'REddyProc' (Reichstein et al., 2005), and displayed the gap-filled results in Fig. S1.

The flux FP was calculated using the simple footprint parameterization model developed by Kljun et al. (2004). Day and night periods were separated using the potential radiation, based on the latitude and longitude, greater and less than 10 W m^{-2}, respectively.

2.3. Bottom-up emissions data

There is always a discrepancy in the estimations between the top-down (flux measurements) and bottom-up (inventory datasets) approaches. One of the valuable uses of tall flux measurements is to estimate the difference by finding the potential locations of sources. To achieve this goal by inter-comparison, we adopted the monthly Open-source Data Inventory for Anthropogenic CO_2 for 2015 (ODIAC, Oda and Maksyutov, 2011; Oda et al., 2018), with a 1-km resolution, and the hourly Fossil Fuel Data Assimilation System for 2015 (FFDAS; http://ffdas.rc.nau.edu/Data.html), with a 10-km resolution. We compared our measured FCO_2 within the area of 90% FP and then compared each of these two CO_2 emissions data.

In addition, we created a local anthropogenic CO_2 emissions dataset using the monthly averaged power-usage-by-contract-type data from the Korea Electric Power Corporation (KEPCO), which consists of seven contract-types, namely street-lamp, late-at-night, education, agricultural, industrial, residential, and general usage. We then retrieved individual building polygons using GIS data from the National Spatial Data Infrastructure portal (NSDI; http://data.nsdi.go.kr/dataset/12623) of the Ministry of Land, Infrastructure, and Transport, which is categorized by the usability of buildings. The total CO_2 emissions were calculated as follows:

$$\text{Total } CO_2 \text{ emissions} = \sum_{k=1}^{l} \left\{ B_i^k \times \left(\sum_{j=1}^{n} E_j^k \div \sum_{j=1}^{n} H_j^k \right) \right\} \times C \tag{2}$$

where B_i^k is the individual building polygons (i) retrieved by GIS, E_j is the monthly averaged power usage of each contract type (j) from KEPCO, and H_j is the number of houses in the contract in each administrative unit (k). These parameters are listed in Table S3. Here, C, provided by KEPCO, is the national constant (424), which converts the power usage (unit: kWh) to the emissions (unit: gCO_2). Finally, GIS extracted the total CO_2 emissions within the FP. Note that we excluded street-lamp and late-at-night contract types in this study because they could not be detected by GIS.

3. Results and discussion

3.1. Meteorological observations

Fig. 2 shows the monthly averaged meteorological variables, including temperature, relative humidity (RH), and winds at three different measurement levels, and solar radiation and total precipitation at the ground level. The temperature showed a typical seasonal variation: the highest in summer (28.6 °C in August) and lowest in winter (2.0 °C in January). The shortwave radiation, one of the main drivers of the biospheric contribution of CO_2, ranged from a minimum of ~0.7 MJ m^{-2} in summer to a maximum of ~0.98 MJ m^{-2} in winter. The highest and lowest values of the averaged RH appeared in the summer (~83%) and winter (57%), respectively, correlated with the seasonal variation in the total accumulated precipitation. The monthly averaged wind speed ranged from ~2.8 (summer) to ~4.5 m s^{-1} (winter); its offset between the 60-m and 300-m levels showed 1.6 and 2.4 m s^{-1} in summer and winter, respectively, due to the mixed sea-land and valley-mountain breeze resulting from the complicated topography surrounding the site.

The average diurnal variation in the meteorological factors presented a typical pattern. The maximum and minimum temperatures appeared around 14:00 (Local Standard Time, LST), approximately 2 h after the peak in the solar radiation, and around 06:00 LST, just before sunrise, respectively. The temperature decreased, along with the measurement height, during the daytime, and vice versa. As expected, the RH showed a notable opposite correlation with the diurnal pattern of temperature, and it decreased with height, showing an average difference of ~15% between 60-m and 300-m levels at night. Wind speeds at 60 m sharply increased in the morning (~8:00 LST), attained a broad maximum in the mid-afternoon (~15:00 LST), and decreased near sunset. The diurnal waves at the higher levels were similar, but with a reduced amplitude. The diurnal wave of wind speed is expected to become nearly 180° out of phase above the surface layer over flat homogeneous areas (Arya, 2000). However, we did not detect phase changes with the height, which is likely due to the relatively heterogeneous topographical features.

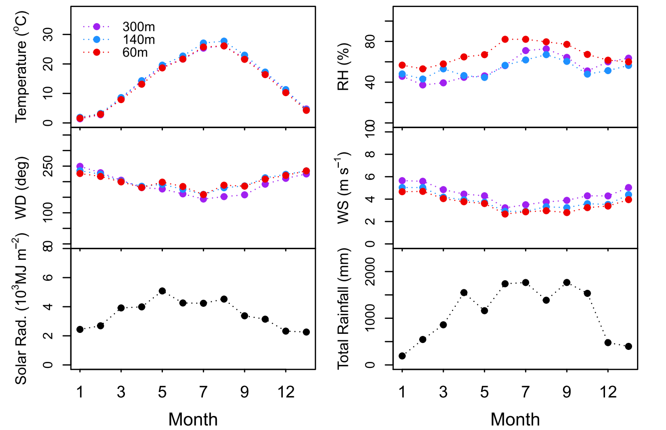

Fig. 2. Monthly averaged variation in the sonic temperature, RH, and wind direction and speed at 60-m, 140-m, and 300-m levels, and the monthly accumulated solar radiation and rainfall on the ground.

3.2. Footprint probability

The FP areas vary depending on the atmospheric stability, surface roughness, and measurement height, among other factors (e.g., Kljun et al., 2004; Kormann and Mexiner, 2006). The surface layer should remain stable or near-neutral in the nighttime and unstable during the daytime. The atmospheric stability parameter (z/L, where L is the Obukhov length and z is the effective measurement height ($z = z_m - d$, where z_m and d are the measurement and displacement heights, respectively) is classified as unstable ($z/L < -0.1$), near neutral ($-0.1 \leq z/L < +0.1$), and stable ($z/L > +0.1$). The ratio z/L affects the estimate of the FP areas, which is the spatial probability distribution that surface sources contribute to the measured fluxes at the tower.

Fig. 3 shows the averaged 90% FP at each level under the condition of $u^* > 0.2$ m s^{-1} at three levels in summer (July) and winter (January). The FP coverage varies depending on the seasonal stability and measurement height. The estimated FP at 60 m (hereafter, FP^{60m}) covered the area with a ~2 km radius from the site, i.e., relatively homogeneous crop paddy fields. FP^{140m}, within a radius of ~4 km, reached farther residential areas located along the mountain skirt in the N and W directions, and an ocean bay in the SE. FP^{300m} covered an area with a radius ranging from 8 to 9 km in the summer and 6–8 km in the winter. These FP ranges were theoretically estimated under the condition of flat homogeneous areas (Kljun et al., 2004). However, the mountain to the N limits both FP^{140m} and FP^{300m} to a radius of < 6 km from the site to the mountain (height: ~520 m). Overall, these different FP coverages, depending on the measurement height, can introduce CO_2 source differences. The contribution of anthropogenic CO_2 emissions is discussed in later sections.

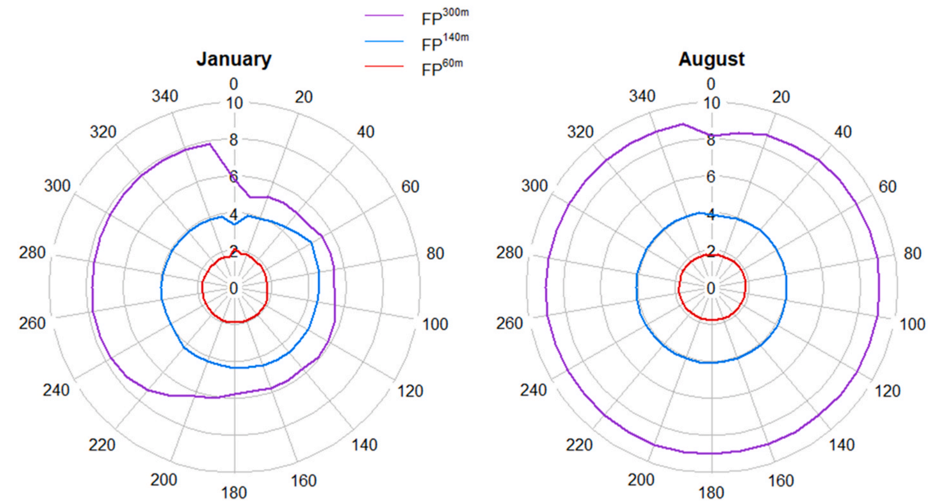

Fig. 3. Spatial distribution of the modeled FP by Kljun et al. (2004) under the condition of u* > 0.15 m s^{-1} in January (left) and July (right).

3.3. CO_2 mixing ratios

The 5-yr consecutive daily averaged CO_2 mixing ratios measured at all three levels are displayed in Fig. S2. The annual mean mixing ratios decreased and increased around 2017, coincident with the CO_2 background measured at Tae-Ahn Peninsula (TAP) in South Korea but a contrast to the trend observed at Mauna Loa, Hawaii, presenting a continuous increasing pattern. The amplitude of daily averaged mixing ratios was 107.2 ppm (60 m), 93.6 ppm (140 m), and 123.8 ppm (300 m) during the study period. The upper two levels (140 m and 300 m) show lower values (< 390 ppm) in summer, as expected, while the lowest level (60 m) presents a continuously increasing trend since 2016.

Fig. 4 displays the monthly averaged CO_2 mixing ratios at three levels in each season. Overall, the mixing ratios decreased with an increasing height. The CO_2 at upper two levels showed a typical seasonal pattern—lower in the summer and higher in the winter—mainly driven by variations in the annual biospheric contribution, solar radiation and anthropogenic emissions. At the 60-m level, in contrast, the mixing ratio showed two dominant peaks in the summer and autumn, likely due to the direct effects of agricultural activities, such as tracker operations and intermittent slash-and-burn around the measurement site. From January to March, the mixing ratio at 140 m was ~4 ppm higher than that at 60 m. The differences in the average mixing ratio between the 60-m and 140-m levels and between the 140-m and 300-m were ~10 and ~7 ppm, respectively, during the entire study period.

Fig. 5 displays the averaged diurnal variation at all three levels in each season, and then the seasonal averaged mixing ratios are reported in Table 2. The diurnal variation in the CO_2 mixing ratio showed a typical pattern: high in the nighttime and low in the daytime. The CO_2 mixing ratios at 60 m and 140 m showed a peak in the early morning around 08:00 LST and then decreased continually; this trend is associated with the increase in both the planetary boundary layer height (PBLH) and biospheric contribution until their minima at 18:00 LST. The CO_2 then increased again until early next morning due to the decrease in PBLH and CO_2 uptake during the nighttime. The amplitude of the CO_2 mixing ratios was 16.2, 9.2, and 7.0 ppm on average at 60 m, 140 m, and 300 m, respectively. Interestingly, the morning peaks at the 300-m level appeared ~2 h later, which implies that the sources were farther from the site and required an extended period to reach a higher level.

The vertical profile of the trace gas mixing ratios observed at multi-level points can provide a feature of the micrometeorology. During the daytime, CO_2 can be mixed well vertically up to the top of the PBL, and all measurement levels can exist within the mixed layer, such that the daytime mixing ratios can have less of a difference among the vertical

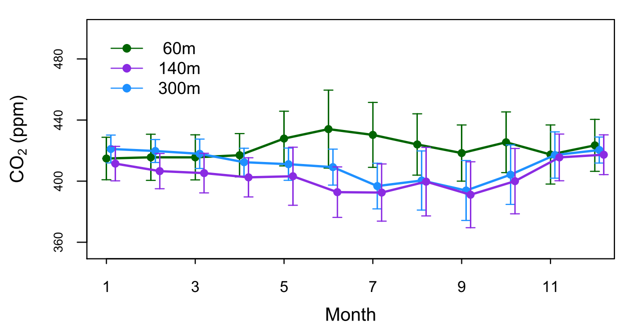

Fig. 4. Monthly averaged CO_2 concentrations with the ±1-σ sd (vertical lines) during the study period.

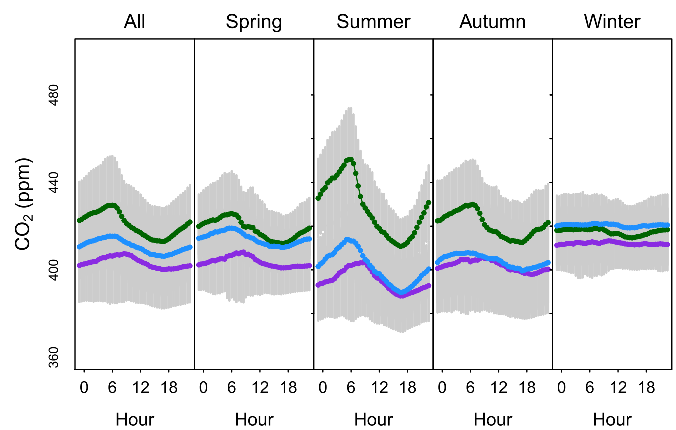

Fig. 5. Diurnal averaged CO_2 concentrations in all and each season. Gray vertical lines are the overlapped ±1-σ sd of each measurement level.

Table 2
Seasonal averaged CO_2 concentrations in each measurement level.

Seasons	Concentration (ppm) ± s.d.		
	60-m	140-m	300-m
Spring	418.6 ± 16.1	414.4 ± 10.1	403.7 ± 15.3
Summer	428.3 ± 22.1	401.4 ± 16.9	395.2 ± 19.9
Autumn	420.6 ± 19.6	404.5 ± 20.6	401.9 ± 22.0
winter	421.0 ± 11.0	418.7 ± 8.5	409.2 ± 12.3
Total	420.7 ± 18.8	410.9 ± 16.7	403.4 ± 16.7

levels. After sunset, the surface cools and forms a stable (nocturnal) boundary layer (SBL) near the ground and a residual layer (RL) just above the SBL (Stull, 1988). When ground emissions are dominant, CO_2 can be trapped within the SBL, such that one can expect to observe higher mixing ratios than that in the RL during the nighttime. Theoretically, unless there are sources located above the SBL, the RL can have a similar mixing ratio as that during the daytime.

In all seasons, except winter, CO_2 at 60 m showed high concentrations, mainly attributed to agricultural activities. Typically, it is expected that CO_2 is well mixed and shows a small vertical gradient in daytime. In spring, CO_2 at 60-m and 140-m showed the lowest values in the daytime because the two levels were in the well-mixed layer, and they presented the highest difference at nighttime. This is likely because the 60-m level was within the SBL and the 140-m level was in the RL. Therefore, the top of the SBL could notably be placed within 60 m and 140 m. This estimated SBL height is in agreement with the results of a previous numerical simulation study that used the Weather Forecasting and Research (WRF) model over the study domain in the spring (Park et al., 2020), which reported that the nighttime inversion layer height may be ~100 ± 20 m around the site. In winter, the CO_2 mixing ratio showed a relatively flat diurnal pattern, mainly caused by the lower amplitude of diurnal variations of PBLH. In contrast to other seasons, the mixing ratio at 140 m was ~3 ppm (on average) higher than 60 m. This flipped-over pattern was mainly affected by winter data in 2007, because of the large number of missing data at 140 m. A further intense study likely needs combining with numerical simulations, such as Crawford et al. (2016).

We also analyzed the temporal aspects of the CO_2 mixing ratio depending on the wind direction (not shown). Higher mixing ratios appeared at all levels in all wind directions, among which there were notable peaks in the N and NE from late autumn to early spring. Flux directionality is useful for investigating the potential source locations, specifically for fluxes, which is discussed in the following section.

3.4. *CO_2 fluxes*

We displayed the 5-yr consecutive daily averaged fluxes before gap-fillings in Fig. S3. During the whole study period, the CO_2 fluxes show typical seasonal variations. The lower two levels clearly showed the significant CO_2 uptake, which coincides with the barley and rice cultivation season in summer and autumn, respectively. Most of their FPs cover crop fields (Fig. 1). The amplitude of daily averaged fluxes was 11.87 μmol m^{-2} s^{-1} (60 m) and 10.53 μmol m^{-2} s^{-1} (140 m). Unlike the lower levels, the fluxes at 300 m did not show a clear biospheric contribution because it was blended by anthropogenic emissions from FP^{300m}, leading to a relatively lower amplitude ~9.00 μmol m^{-2} s^{-1}.

3.4.1. *Temporal variation and vertical profile*

In this section, we discuss the characteristics of our measured CO_2 fluxes over the barley–rice double-crop fields. In general, crop cultivation consists of several stages, including germination (or emergence, B1), seedling and winter rest (B2), tillering (B3), and ripening (B4) for barley cultivation; and transplanting (or rooting, R1), tillering (R2), elongation (R3), and ripening (R4) for rice cultivation (e.g., Shim et al., 2016; Min et al., 2014). For the convenience of analysis, we divided the flux time series into three stages: (1) the barley-growing period (hereafter, BAR), including both B3 and B4, from February 28 to May 21, (2) the rice-growing period (RIC), including R2, R3, and R4, from June 16 to October 19, and (3) the non-growing period (OTH), from Rh to B2 (from late October to late February) and from Bh to R1 (from late May to mid-June). The dates of each stage were provided by the Agricultural Technical Center in Boseong-gun (personal communication), which are reported in Table 3 with the averaged FCO_2 in each cultivation stage. There were almost no fallow days around the BSWO. When the barley harvest is completed, farmers begin to successively transplant rice. The starting and ending days of each stage can have maximum offset of 5 d,

Table 3
Averaged FCO_2 in each crop cultivation stage at all three levels, after gap-filling.

Crop type	Stage	FCO_2 (μmol m^{-2} s^{-1})		
		60-m	140-m	300-m
Barley	B1	2.71 ± 7.77	2.19 ± 6.16	1.88 ± 8.39
	B2	0.70 ± 5.17	1.52 ± 5.79	1.59 ± 6.84
	B3	−1.43 ± 6.91	−1.10 ± 7.44	−0.13 ± 7.90
	B4	1.99 ± 9.84	0.18 ± 6.24	0.59 ± 9.65
	Bh	−0.83 ± 11.12	0.03 ± 9.78	0.57 ± 10.63
Rice	R1	1.76 ± 6.50	1.43 ± 9.93	1.67 ± 8.23
	R2	−0.18 ± 10.58	0.77 ± 8.05	0.72 ± 10.28
	R3	−2.88 ± 13.15	−1.50 ± 10.60	0.91 ± 12.27
	R4	−0.90 ± 10.89	0.13 ± 10.48	0.07 ± 10.84
	Rh	2.26 ± 6.69	1.69 ± 6.34	1.27 ± 7.85
Total		−0.28 ± 8.81	0.34 ± 8.08	0.79 ± 9.08

mainly depending on the weather and climate conditions as well as the individual circumstances of each farm owner.

FCO_2 is generally expected to show the lowest value in summer, dominated by photosynthesis of the biosphere, and the highest value in winter, due mainly to shedding plant leaves and fossil-fuel emissions. Compared with other levels, FP^{60m} covered the relatively pure homogeneous crop paddy areas. Fig. 6 shows the daily averaged variation in FCO_2 at all three measurement levels throughout the year. It shows a double-deep pattern, as expected, due to barley–rice double-crop cultivation, combined with the variation in the solar radiation and crop growth. Two negative peaks occurred in April and July owing to strong CO_2 uptake during the barley- and rice-growing periods, respectively,

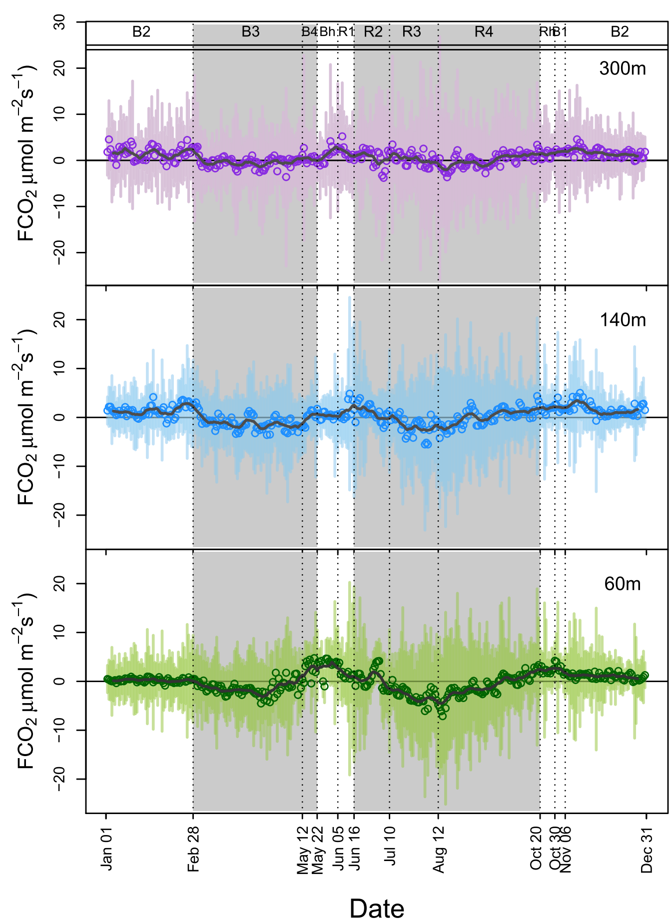

Fig. 6. Daily averaged FCO_2 at three measurement points. Black lines indicate the 10-d moving averages; the shaded areas represent the crop growing periods, including BAR; and the vertical lines indicates ±1-σ sd.

while two positive peaks mainly appeared in the OTH, just after harvesting and before the tillering stages (B3) when the CO_2 uptake by crops was not significant. FCO_2^{60m} showed an almost flat pattern, maintaining positive values in the barley germination stage (B1), as well as the seedling and winter rest stage (B2). As the tillering stage (B3) started, FCO_2 gradually decreased until mid-April and then rapidly increased from the later tillering stage to the ripening stage (B4). In the ripening stage, the sign of the FCO_2 changed to positive the averaged FCO_2^{60m} presented −1.43 μmol m^{-2} s^{-1} (B3) and −1.99 μmol m^{-2} s^{-1} (B4). During the rice cultivation period, in the tillering stage (R2), FCO_2 began to rapidly decrease until mid-August. In the middle of the ripening stage (R4), FCO_2 started to gradually increase until mid-October, while both the solar radiation and biospheric contribution decreased. The averaged FCO_2^{60m} showed −2.88 μmol m^{-2} s^{-1} (R3) to −0.90 μmol m^{-2} s^{-1} (R4).

The amplitude of the fluxes decreased with the height due to the reduction in the biospheric contribution and the increment of anthropogenic effects with the extension of the FP. Fig. 7 shows the averaged diurnal variation in FCO_2 at each of the three levels in BAR, RIC, and OTH. The biospheric contribution of the CO_2 uptake between the BAR and RIC can be estimated by the daytime amplitude of the FCO_2. Compared with the other two upper levels, FCO_2^{60m} showed the highest amplitude, mainly driven by CO_2 uptake over relatively homogeneous paddy fields during the daytime. FCO_2^{60m} began to decrease, changing its sign to negative after ~09:00 LST as the solar radiation increased. After noon, the flux increased until ~18:00 LST, and then its sign changed to and remained positive throughout the night until the next morning. The averaged biospheric contributions of barley and rice were −3.40 and −4.88 μmol m^{-2} s^{-1}, respectively, in the daytime. The CO_2 uptake by rice was, on average, about one third more than that by barley during the BAR and RIC. During the nighttime, the fluxes ranged from −0.06 to 1.93 μmol m^{-2} s^{-1} (IQR), which implies that nighttime anthropogenic effects were not significant within FP^{60m}.Overall, the crop field played the role of a net absorber of CO_2 during both the BAR and RIC.

The magnitude of the daytime FCO_2 decreased with height, as the anthropogenic emissions affected the measured fluxes. FCO_2^{300m} gradually decreased and rapidly increased, before and after ~16:00 LST, respectively, implying that the measured fluxes were continually affected by anthropogenic emissions during working hours. Considering the complicity of the sources in FP^{300m}, the more accurate locations of the potential sources can be identified using the flux dependency based on the wind directions, which is discussed in section 3.4.3.

At all three levels, FCO_2 showed mostly positive values due to the lack of CO_2 uptake by crops in OTH. The averaged FCO_2^{60m}, FCO_2^{140m}, and FCO_2^{300m} were positive values: 1.02 (IQR: -0.32–2.06), 1.49 (IQR: -0.36 – 2.93), and 1.58 μmol m^{-2} s^{-1} (IQR: -0.70 - 3.18 μmol m^{-2} s^{-1}), respectively. These values from the long-term measurements can be simply interpreted as the background fluxes around the site, specifically within the FP areas of each measurement level. Although roads are also included within the FP^{300m}, there is no clear evidence of rush-hour peaks, which is unlikely in urban areas (e.g., Velasco et al., 2005; Park and Schade, 2016). This is coincident with the time lag (~2 h) of the morning peak in the CO_2 mixing ratio, which was caused by sources far from the site, as described in section 3.3.

3.4.2. Relation with radiation and temperature

In this subsection, we discuss the relationship between FCO_2 and meteorological factors. These factors include solar radiation, mainly driving biospheric CO_2 uptake, and nighttime air temperature, strongly linked to respiration. We focus on the data measured at 60 m because its FPs mostly cover relatively homogeneous areas.

Fig. 8 shows the relationship between the FCO_2 and solar radiation in BAR, RIC, and OTH. In both crop-growing periods, FCO_2 exponentially decreased as the solar radiation increased up to ~1,600 (for barley) and ~1,900 μmol m^{-2} s^{-1} (for rice), after which it rebounded and increased slightly. The points of inflection may represent the saturation points of the response to solar radiation. When the solar radiation at > 800 μmol m^{-2} s^{-1}, the gradient of CO_2 uptake in the RIC was steeper than that in the BAR. This difference was likely due to the biospheric contribution of each crop: the biospheric contribution of rice was ~40% higher than that of barley at 1,600 μmol m^{-2} s^{-1} based on the best-fit curve. In contrast to the growing periods, FCO_2 remained almost constant in the OTH. Thus, it is not related with the solar radiation because the crops are not grown enough to significantly uptake CO_2, specifically in the barley germination and seedling and rice transplanting stages.

Fig. 9 displays the relationship between FCO_2^{60m} and nighttime air

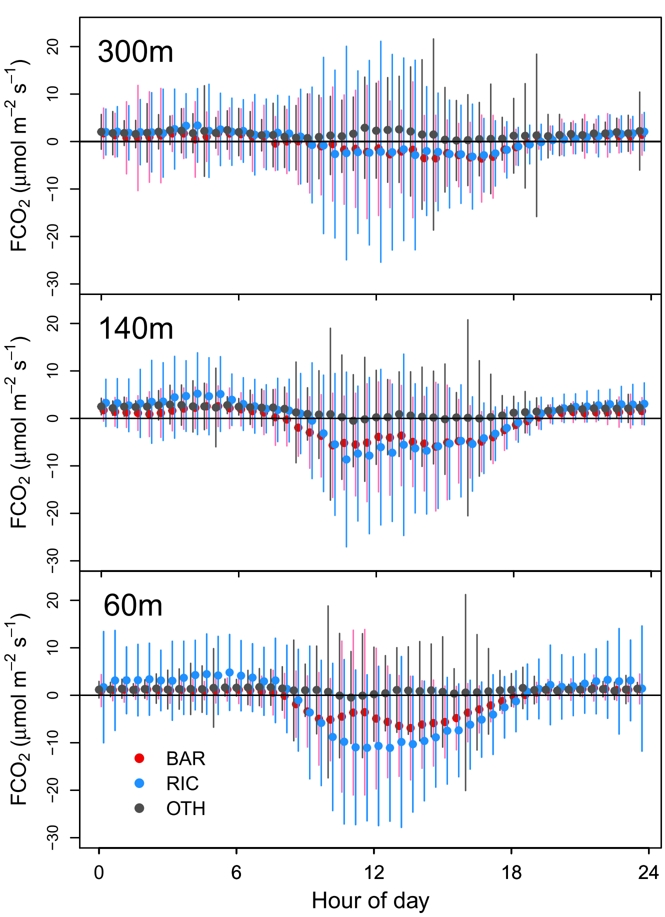

Fig. 7. Averaged diurnal variations in the FCO_2 at three measurement levels in BAR, RIC, and OTH. Vertical lines indicate ±1-σ sd.

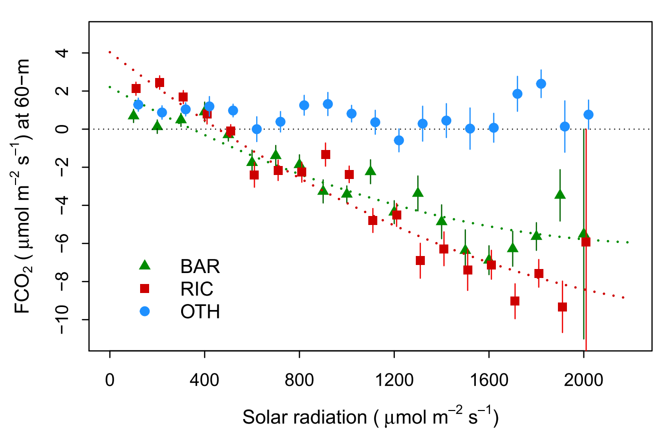

Fig. 8. Relationship between the solar radiation and FCO_2^{60m} during BAR, RIC and OTH in daytime, using data binned into 100 μmol m^{-2} s^{-1} intervals. The vertical bars indicate ±1-σ standard errors.

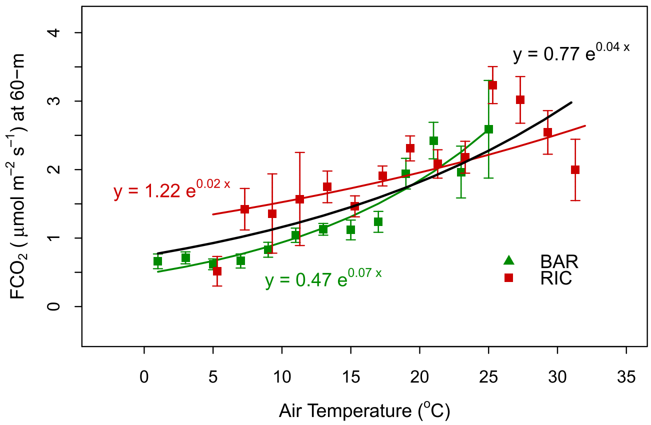

Fig. 9. Relationship between the temperature and FCO_2^{60m} in nighttime using data binned into 2 °C intervals with standard errors. Green, red, and black curves indicate the simulated response functions with a Q_{10} of 1.97, 1.28, and 1.57, respectively. (For interpretation of the references to colour in this figure legend, the reader is referred to the Web version of this article.)

temperature for both the BAR and RIC. Overall, FCO_2 increased exponentially with the increase in air temperature. The response rate slope was mostly higher in the BAR than that in the RIC, but the absolute magnitude of respiration was higher in the RIC. We evaluated the FCO_2 response to temperature, calculating Q_{10} for this study area using a typical respiration Q_{10} model (Atkin et al., 2005; von Lutzow and Koegel-Knabner, 2009). The Q_{10} factors were 1.97 and 1.28 for barley and rice, respectively, which were relatively low and could represent local autotrophic respiration to higher ambient temperature (Smith and Dukes, 2013) in this cropland. Due to the irrigation control system for rice cultivation, we did not find a reduction in heterotrophic respiration, which is related to circumstances under drought.

3.5. FCO_2 wind direction dependency

For the application of the tall tower measurement system, finding potential CO_2 sources at the local scale using direct flux measurements is critical. We identified the sources with a combination of wind direction and footprint analysis as well as GIS techniques. We analyzed the directionality of fluxes as displayed in Fig. 10: (a) the monthly pattern and (b) the diurnal variation for the OTH. Focusing only on the OTH can minimize the contribution of crops, such that we can monitor the anthropogenic emissions affecting the measurement points. We retrieved individual building polygons, using the GIS tool, within each level's FP area.

Relatively large FCO_2 (> 4 μmol m^{-2} s^{-1}) appeared in the directions from N to SE for all three levels in the winter and additionally in the NW at the 60-m and 140-m level in the summer. The winter peaks were likely from various potential sources, including a large number of factory buildings, warehouses, and various facilities, and relatively densely populated residential areas within each FP level. The GIS analysis did not reveal any other significant potential sources in the study area.

For FP^{60m}, specifically, GIS detected ~20 factories and residential areas (consisting of 358 houses) at ~2 km in the directions ranging from 290° to 340°, which were likely the main sources for the dominant peaks in the FCO_2^{60m} and FCO_2^{140m} in the NW during the summer (Fig. 10). Additional peaks emerged around May in the SE, although there are no building-type potential sources in this direction. A further survey revealed that the winter fluxes originated from fishery boasts for the aquaculture industry at the edge of FP^{60m} in the SE (Fig. 1), which could not be detected by GIS. During the OTH, the emissions from boasts notably occurred in the early morning and were more dominant in the upper-level FPs (Fig. 10(b)).

More complicated heterogeneous sources can be included in the

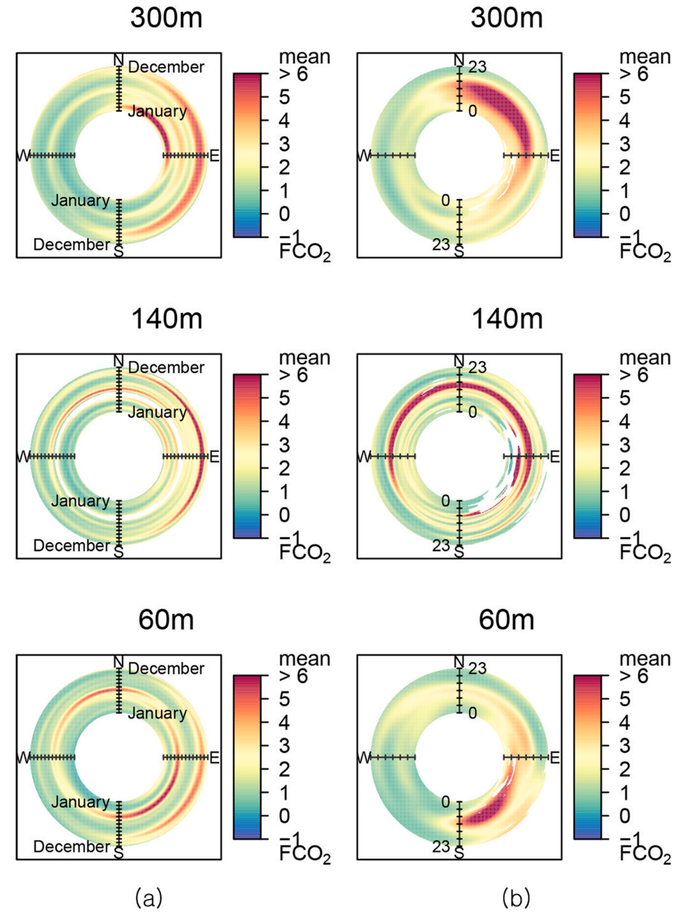

Fig. 10. Fluxes at each level with respect to wind direction: (a) monthly averaged for the entire study period and (b) diurnal mean only for the OTH (unit: μmol m^{-2} s^{-1}).

higher level FPs. The potential sources of significant FCO_2^{140m} were likely from ~20 factory buildings and residential houses, located ~3.8 km in the directions ranging from 20° to 80°, and those for FCO_2^{300m} were mostly attributed to ~50 factories, especially the Joseong Agricultural and Industrial Complex (~6.5 km in the direction of 30°), which is one of the largest industrial sources within FP^{300m}.

Fig. 10(b) shows the diurnal wind directionality in the OTH, with the time of the day and direction of potential emissions. This indicates that the dominant FCO_2^{140m} and FCO_2^{300m}, which appeared in NE during the daytime, can be mainly attributed to the industry area, as described in the previous paragraph.

GIS can successfully retrieve anthropogenic sources, such as factories and residential houses, and it is useful in collecting emissions sources for the bottom-up approach. However, it is not possible to find no-building-type sources, such as fishery boats for the aquaculture industry in the ocean bay, and agricultural activities, such as slash-and-burn fields and tracker operations. These types of sources are generally missing or underestimated in emissions inventories. They can only be detected by direct flux measurements. In the next section, we discuss the quantitative estimation of the offset in the study area.

3.5.1. Comparison with the bottom-up approach

There are always gaps between the top-down (i.e., flux measurements) and bottom-up (i.e., emissions inventory) approaches. In this subsection, we attempted to investigate the gap between the two approaches in our study area. We compared the measured fluxes estimated within the 90%-FP^{300m} (approx. 227 km^2), for which the local anthropogenic CO_2 emissions dataset was constructed by the method described in section 2.3. We focused only on the period of the OTH to minimize the biospheric effects.

The averaged FCO_2 was ~14,750 tons CO_2 $month^{-1}$ (std. error 1,302 ton CO_2 $month^{-1}$) within FP^{300m} during the OTH. The CO_2 emissions of ODIAC within an area of 8 km × 8 km at the center of the site were underestimated by ~69%, and those of FFDAS at a point near BSWO were underestimated by ~46% compared with the mean value. Our CO_2 emissions dataset, based on KEPCO power-usage-contract-type data, showed 9,021 ton CO_2 $month^{-1}$, which is underestimated by approximately 31%. Previous studies (Turbull et al., 2011; Asefi-Najafabady et al., 2014) reported that bottom-up approaches usually yield large uncertainties of ~50– 200% in urban areas. Considering that our study area can range from cropland to suburban areas, our uncertainty is acceptable.

These underestimations are likely due to missing sources and/or underestimated emissions in the process of the development of the emissions inventory. For example, sources emitting lower than a criteria value generally do not have a mandatory reporting emission, such as from fishery boasts in the SE (section 3.4.2). Some source owners may provide underestimated emissions on purpose or by mistake. Although the underestimation of our local CO_2 emissions dataset based on the electric-power-usage data had the lowest magnitude, it may have a few limits. The electric power usage cannot guarantee that the actual CO_2 emission source is within the FP because power plants are generally located far outside or in another administrative unit to avoid local air pollution. In the case of FP^{300m}, there are only six small solar power plants. For a more precise estimate of the emissions, we must use a 2D footprint model (e.g., Kormann and Mexiner, 2001), with which we can calculate the spatial footprint probability at each surface pixel and weight to the measured flux.

4. Conclusion and summary

In this study, we investigated the characteristics of the CO_2 mixing ratios and fluxes monitored at a tall tower, located in the center of a barley-rice double-crop paddy field in Boseong-gun, Jeollanam-do, South Korea, with three different measurement levels (60 m, 140 m, and 300 m) over a 5-yr period from July 2015 to December 2019. The CO_2 mixing ratios at higher levels (140 m and 300 m) showed a typical seasonal pattern, i.e., lower in the summer and higher in the winter, while those at 60 m were higher in the summer and autumn due to the effects of agricultural activities near the surface during the cultivation season. The averaged diurnal variations in CO_2 during each season revealed that the difference in significant nighttime mixing ratios at each measurement level was mainly caused by the distinct wind directions.

The measured FCO_2 showed two dominant negative peaks in April and August, mainly driven by the barley and rice CO_2 uptake, respectively. The flux amplitudes decreased with the increase in height as the FP areas extended and covered more anthropogenic sources. The relationship between FCO_2 and solar radiation showed a decreasing pattern mainly by crop contributions. The light saturation point was ~1,600 (BAR) and ~1,900 μmol m^{-2} s^{-1} (RIC), and rice likely absorbed ~40% more CO_2 than barley at 1,600 μmol m^{-2} s^{-1} during the study period. The response of the FCO_2 to nighttime air temperature was estimated at the Q_{10} value, which was 1.97 and 1.28 for barley and rice, respectively. The relatively lower Q_{10} value for rice is a feature of local autotrophic respiration, typically in irrigation fields.

We attempted to find the locations of the potential sources using an analysis of the flux dependency on the wind directions combined with GIS techniques. We found that the dominant peaks appeared from the NW to E directions within the FPs, where not only residential houses, but also many factories and industrial complexes are distributed. The wind directionality revealed peaks in the SE, whose potentially attributed to fishery boats for the aquaculture industry, which were not detectable by GIS because they were not building-type sources. Finding missing sources in the bottom-up approach is one of the most significant advantages of direct flux measurements in the field. The CO_2 emissions from ODIAC and FFDAS were underestimated by ~69% and 46%, respectively. Our bottom-up emission dataset, based on the electric-power-usage from KEPCO, was underestimated by ~31% within FP^{300m} during the OTH.

In summary, techniques used to detect potential sources using the flux dependency based on wind directions (section 3.4.3) can be combined with techniques used to estimate the underestimation of bottom-up approaches to find and monitor hidden CO_2 sources at a local scale. This will help in the management of local CO_2 emissions and establishment of environmental policies for international cooperation to prevent global warming. To further improve the results for the estimation of anthropogenic sources, we will conduct further studies using a source apportionment of anthropogenic and biogenic sources (Park and Schade, 2016) and a quadrant analysis (Werner, 2013) with the 2D FP model (e.g., Kormann and Mexiner, 2001).

CRediT authorship contribution statement

Changhyoun Park: Conceptualization, Methodology, Writing – original draft, Data curation, Investigation. **Young-Tae Lee:** Resources. **Soon-Hwan Lee:** Investigation, Writing – review & editing, Supervision, Project administration.

Declaration of competing interest

The authors declare that they have no known competing financial interests or personal relationships that could have appeared to influence the work reported in this paper.

Acknowledgment

This study was supported by the Basic Science Research Program through the National Research Foundation of Korea (NRF) funded by the Ministry of Education (2020R1A6A1A03044834) of South Korea. We thank the researchers at National Institute of Meteorological Sciences (NIMS) for access to observation data in Boseong Standard Weather Observatory (BSWO) for providing the measurement data, and Dr. Kevin R. Gurney at Northern Arizona University for FFDAS emission dataset.

Appendix A. Supplementary data

Supplementary data to this article can be found online at https://doi.org/10.1016/j.atmosenv.2021.118340.

References

Arya, P.S., 2001. Introduction to Micrometeorology. Academic Press, pp. 101–209 (Chapter 6).

Asefi-Najafabady, S., Rayner, P.J., Gurney, K.R., McRobert, A., Song, Y., Coltin, K., Huang, J., Elvidge, C., Baugh, K., 2014. A multiyear, global gridded fossil fuel CO2 emission data product: evaluation and analysis of results. J. Geophys. Res. Atmos. 119.

Atkin, O.K., Bruhn, D., Hurry, V.M., Tjoelker, M.G., 2005. The hot and the cold: unravelling the variable response of plant respiration to temperature. Funct. Plant Biol. 32, 87–105.

Bakwin, P.S., Tans, P.P., Zhao, C.L., Ussler, W., Quesnell, E., 1995. Measurements of carbon-dioxide on a very tall tower. Tellus B 47, 535–549.

Bakwin, P.S., Tans, P.P., Hurst, D.F., Zhao, C.L., 1998. Measurements of carbon dioxide on very tall towers: results of the NOAA/CMDL program. Tellus B 50, 401–415.

Baldocchi, D., Falge, E., Gu, L.H., Olson, R., Hollinger, D., Running, S., Anthoni, P., Bernhofer, C., Davis, K., Evans, R., Fuentes, J., Goldstein, A., Katul, G., Law, B., Lee, X.H., Malhi, Y., Meyers, T., Munger, W., Oechel, W., U, K.T.P., Pilegaard, K., Schmid, H.P., Valentini, R., Verma, S., Vesala, T., Wilson, K., Wofsy, S., 2001. FLUXNET: a new tool to study the temporal and spatial variability of ecosystem-scale carbon dioxide, water vapor, and energy flux densities. Bull. Am. Meteorol. Soc. 82, 2415–2434.

Crawford, B., Christen, A., and McKendry, I., Diurnal course of carbon dioxide mixing ratios in the urban boundary layer in response to surface emissions, J. Appl. Meteorol. Clim., 55(3), 507-529.

Davis, K.J., Bakwin, P.S., Yi, C.X., Berger, B.W., Zhao, C.L., Teclaw, R.M., Isebrands, J.G., 2003. The annual cycles of CO2 and H2O exchange over a northern mixed forest as observed from a very tall tower. Global Change Biol. 9, 1278–1293.

Falge, E., Baldocchi, D., Tenhunen, J., Aubinet, M., Bakwin, P., Berbigier, P., Bernhofer, C., Burba, G., Clement, R., Davis, K.J., Elbers, J.A., Goldstein, A.H., Grelle, A., Granier, A., Guomundsson, J., Hollinger, D., Kowalski, A.S., Katul, G., Law, B.E., Malhi, Y., Meyers, T., Monson, R.K., Munger, J.W., Oechel, W., Paw, K.T., Pilegaard, K., Rannik, U., Rebmann, C., Suyker, A., Valentini, R., Wilson, K., Wofsy, S., 2002. Seasonality of ecosystem respiration and gross primary production as derived from FLUXNET measurements. Agric. For. Meteorol. 113, 53–74.

Fan, S.M., Wofsy, S.C., Bakwin, P.S., Jacob, D.J., Fitzjarrald, D.R., 1990. Atmosphere-biosphere exchange of CO_2 and O_3 in the Central Amazon Forest. J. Geophys. Res. 95, 16851–16864.

Gash, J.H.C., Culf, A.D., 1996. Applying a linear detrend to eddy correlation data in real time. Bound-Lay Meteorol. 79, 301–306.

Grimmond, C.S.B., Salmond, J.A., Oke, T.R., Offerle, B., Lemonsu, A., 2004. Flux and turbulence measurements at a densely built-up site in Marseille: heat, mass (water and carbon dioxide), and momentum. J. Geophys. Res. Atmos. 109.

Gurney, K.R., Mendoza, D.L., Zhou, Y.Y., Fischer, M.L., Miller, C.C., Geethakumar, S., Du Can, S.D., 2009. High resolution fossil fuel combustion CO2 emission fluxes for the United States. Environ. Sci. Technol. 43, 5535–5541.

Horst, T.W., Weil, J.C., 1992. Footprint estimation for scalar flux measurements in the atmospheric surface-layer. Bound-Lay Meteorol. 59, 279–296.

Ibrom, A., Dellwik, E., Larsen, S.E., Pilegaard, K., 2007. On the use of the Webb-Pearman-Leuning theory for closed-path eddy correlation measurements. Tellus B 59, 937–946.

IPCC, 2013. Climate Change 2013: The Physical Science Basis. Contribution of Working Group I to the Fifth Assessment Report of the Intergovernmental Panel on Climate Change [Stocker, T.F., D. Qin, G.-K. Plattner, M. Tignor, S.K. Allen, J. Boschung, A. Nauels, Y. Xia, V. Bex and P.M. Midgley (eds.)]. In: Cambridge University Press, Cambridge, United Kingdom and New York, NY, USA, p. 1535. https://www.ipcc.ch/report/ar5/wg1/#:~:text=Report-,The%20Working%20Group%20I%20contribution%20to%20the%20Fifth%20Assessment%20Report,Report%20(AR4)%20was%20released.

Kim, H., Hong, J-W, Lim, Y-J, Hong, J, Shin, S-S, Kim, Y-J, 2019. Evaluation of JULES land surface model based on in-situ data of NIMS flux sites. Atmosphere 29 (4), 355–365. https://doi.org/10.14191/Atmos.2019.29.4.355. https://www.koreascience.or.kr/article/JAKO201907963545168.page.

Kim, M.S., Kwon, B.H., 2019. Estimation of sensible heat flux and atmospheric boundary layer height using an unmanned aerial vehicle. Atmosphere 10 (7), 363. https://doi.org/10.3390/atmos10070363. https://www.mdpi.com/2073-4433/10/7/363.

Kim, W., Yum, S.S, Hong, J., Song, J.I., 2020. Improvement of fog simulation by the nudging of meteorological tower data in the WRF and PAFOG coupled model. Atmosphere 11 (3), 311. https://doi.org/10.3390/atmos11030311. https://www.mdpi.com/2073-4433/11/3/311#cite.

Kljun, N., Calanca, P., Rotach, M.W., Schmid, H.P., 2004. A simple parameterisation for flux footprint predictions. Bound-Lay Meteorol. 112, 503–523.

Kormann, R., Meixner, F.X., 2001. An analytical footprint model for non-neutral stratification. Bound-Lay Meteorol. 99, 207–224.

Le Quere, C., Peters, G.P., Andres, R.J., Andrew, R.M., Boden, T.A., Ciais, P., Friedlingstein, P., Houghton, R.A., Marland, G., Moriarty, R., Sitch, S., Tans, P., Arneth, A., Arvanitis, A., Bakker, D.C.E., Bopp, L., Canadell, J.G., Chini, L.P., Doney, S.C., Harper, A., Harris, I., House, J.I., Jain, A.K., Jones, S.D., Kato, E., Keeling, R.F., Goldewijk, K.K., Kortzinger, A., Koven, C., Lefevre, N., Maignan, F., Omar, A., Ono, T., Park, G.H., Pfeil, B., Poulter, B., Raupach, M.R., Regnier, P., Rodenbeck, C., Saito, S., Schwinger, J., Segschneider, J., Stocker, B.D., Takahashi, T., Tilbrook, B., van Heuven, S., Viovy, N., Wanninkhof, R., Wiltshire, A., Zaehle, S., 2014. Global carbon budget 2013. Earth Syst. Sci. Data 6, 235–263.

Lim, H.-J., Lee, Y.-H., 2019. Characteristics of sea breezes at coastal area in boseong. Atmosphere 29 (1), 41–51. https://doi.org/10.14191/ATMOS.2019.29.1.041. https://www.koreascience.or.kr/article/JAKO201913649330064.page.

Liu, H.Z., Feng, J.W., Jarvi, L., Vesala, T., 2012. Four-year (2006-2009) eddy covariance measurements of CO2 flux over an urban area in Beijing. Atmos. Chem. Phys. 12, 7881–7892.

Mauder, M., Foken, T., 2006. Impact of post-field data processing on eddy covariance flux estimates and energy balance closure. Meteorol. Z. 15, 597–609.

Min, S.H., Shim, K.M., Kim, Y.S., Hwang, H., Jung, M.P., Choi, I.T., 2014. Seasonal variation of CO2 exchange during the barley growing season at a rice-barley double cropping paddy field in Gimje, Korea. Kor. J. Agric. Forest Meteorol. 16, 137–145.

Moncrieff, J.B., Massheder, J.M., deBruin, H., Elbers, J., Friborg, T., Heusinkveld, B., Kabat, P., Scott, S., Soegaard, H., Verhoef, A., 1997. A system to measure surface fluxes of momentum, sensible heat, water vapour and carbon dioxide. J. Hydrol. 188, 589–611.

Moncrieff, J.B., Clement, R., Finnigan, J., Meyers, T., 2004. Averaging, detrending and filtering of eddy covariance time series. In: Lee, X., Massman, W.J., Law, B.E. (Eds.), Handbook of Micrometeorology: a Guide for Surface Flux Measurements. Kluwer Academic, Dordrecht, pp. 7–31.

Nemitz, E., Hargreaves, K.J., McDonald, A.G., Dorsey, J.R., Fowler, D., 2002. Meteorological measurements of the urban heat budget and CO2 emissions on a city scale. Environ. Sci. Technol. 36, 3139–3146.

Oda, T., Maksyutov, S., 2011. A very high-resolution (1 km x 1 km) global fossil fuel CO2 emission inventory derived using a point source database and satellite observations of nighttime lights. Atmos. Chem. Phys. 11, 543–556.

Oda, T., Maksyutov, S., Andres, R.J., 2018. The Open-source Data Inventory for Anthropogenic CO2, version 2016 (ODIAC2016): a global monthly fossil fuel CO2 gridded emissions data product for tracer transport simulations and surface flux inversions. Earth Syst. Sci. Data 10, 87–107.

Park, C., Schade, G.W., 2016. Anthropogenic and biogenic features of long-term measured CO2 flux in north downtown Houston, Texas. J. Environ. Qual. 45, 253–265.

Park, C., Park, S.Y., Gurney, K.R., Gerbig, C., DiGangi, J.P., Choi, Y., Lee, H.W., 2020. Numerical simulation of atmospheric CO2 mixing ratio and flux over the Korean Peninsula using WRF-VPRM model during Korus-AQ 2016 campaign. PloS One 15.

Peylin, P., Rayner, P.J., Bousquet, P., Carouge, C., Hourdin, F., Heinrich, P., Ciais, P., contributors, A., 2005. Daily CO2 flux estimates over Europe from continuous atmospheric measurements: 1, inverse methodology. Atmos. Chem. Phys. 5, 3173–3186.

R Core Team, 2014. R: A Language and Environment for Statistical Computing. R Foundation for StatisticalComputing, Vienna, Austria. URL. http://www.R-project.org/.

Reichstein, M., Falge, E., Baldocchi, D., et al., 2005. On the separation of net ecosystem exchange into assimilation and ecosystem respiration: review and improved algorithm. Global Change Biol. 11, 1424–1439.

Shim, K.M., Min, S.H., Kim, Y.S., Jung, M.P., Choi, I.T., 2015. Estimation of net biome production in a barley-rice double cropping paddy field of Gimje, Korea. Kor. J. Agric. Forest Meteorol. 17, 173–181.

Smith, N.G., Dukes, J.S., 2013. Plant respiration and photosynthesis in global-scale models: incorporating acclimation to temperature and CO2. Global Change Biol. 19, 45–63.

Stull, R.B., 1988. An Introduction to Boundary Layer Meteorology. Atmopsheric and oceanographic sciences library, pp. 9–19.

Tans, P.P., Fung, I.Y., Takahashi, T., 1990. Observational constraints on the global atmospheric Co2 budget. Science 247, 1431–1438.

Turnbull, J.C., Karion, A., Fischer, M.L., Faloona, I., Guilderson, T., Lehman, S.J., Miller, B.R., Miller, J.B., Montzka, S., Sherwood, T., Saripalli, S., Sweeney, C., Tans, P.P., 2009. Assessment of fossil fuel carbon dioxide and other anthropogenic trace gas emissions from airborne measurements over Sacramento, California in spring. Atmos. Chem. Phys. 11, 705–721, 2011.

Velasco, E., Pressley, S., Allwine, E., Westberg, H., Lamb, B., 2005. Measurements of CO2 fluxes from the Mexico City urban landscape. Atmos. Environ. 39, 7433–7446.

Velasco, E., Roth, M., Tan, S.H., Quak, M., Nabarro, S.D.A., Norford, L., 2013. The role of vegetation in the CO2 flux from a tropical urban neighbourhood. Atmos. Chem. Phys. 13, 10185–10202.

Vickers, D., Mahrt, L., 1997. Quality control and flux sampling problems for tower and aircraft data. J. Atmos. Ocean. Technol. 14, 512–526.

von Lutzow, M., Kogel-Knabner, I., 2009. Temperature sensitivity of soil organic matter decomposition-what do we know? Biol. Fertil. Soils 46, 1–15.

Webb, E.K., Pearman, G.I., Leuning, R., 1980. Correction of flux measurements for density effects due to heat and water-vapor transfer. Q. J. Roy. Meteorol. Soc. 106, 85–100.

Werner, N., 2013. Anthropogenic and Biogenic Carbon Dioxide Fluxes from Typical Land Uses in Houston, Texas. Master's thesis. Texas A&M University.

Wilczak, J.M., Oncley, S.P., Stage, S.A., 2001. Sonic anemometer tilt correction algorithms. Bound-Lay Meteorol. 99, 127–150.

Yi, C., Davis, K.J., Bakwin, P.S., Berger, B.W., Marr, L.C., 2000. Influence of advection on measurements of the net ecosystem-atmosphere exchange of CO2 from a very tall tower. J. Geophys. Res. Atmos. 105, 9991–9999.